Article

Modeling of a Rotary Adsorber for Continuous Capture of Indoor Carbon Dioxide

Lumeng Liu [1,2,3], Ning Wan [1,2,3], Wenmao Zeng [1,2,3], Jiachen Shi [1,2,3], Meng Liu [1,2,3] and Huan Liu [1,2,3,*]

[1] School of Civil Engineering, Chongqing University, Chongqing 400045, China; lumeng.liu@cqu.edu.cn (L.L.)
[2] Joint International Research Laboratory of Green Buildings and Built Environments, Ministry of Education, Chongqing University, Chongqing 400045, China
[3] National Centre for International Research of Low-Carbon and Green Buildings, Ministry of Science and Technology, Chongqing University, Chongqing 400045, China
[*] Correspondence: huanliu@cqu.edu.cn

Abstract: Removing indoor CO_2 as a pollutant via solid sorbents is a promising solution to maintaining acceptable indoor air quality while minimizing the energy consumption of ventilation. Compared to fixed-bed and fluidized-bed configurations, which require at least two beds to allow for continuous operation, a rotary adsorber is more compact and suitable to be integrated into the ventilation systems of buildings. In the present study, a regenerative rotary adsorber based on temperature swing adsorption was modeled to investigate continuous CO_2 capture in an indoor environment. The governing equations of heat and mass transfer processes associated with the capture were established and coded in ANSYS Fluent software. The spatiotemporal variations of CO_2 concentration and temperature in gas and solid phases within the rotary adsorber were obtained. The key findings are: (1) adjusting the speed mainly affects circumferential concentration and temperature distribution, but has little impact on axial concentration and temperature; (2) Increasing desorption inlet flow rate has little impact on adsorption outlet concentration, but significantly decreases desorption outlet concentration; (3) Raising desorption inlet temperature can increase both adsorption and desorption outlet average concentrations; (4) Reducing the volume proportion of the desorption sector will slightly increase adsorption outlet concentration and slightly decrease desorption outlet concentration, but barely affects average adsorption and desorption outlet temperatures.

Keywords: air quality; carbon dioxide adsorption; rotary wheel device

1. Introduction

Indoor air quality (IAQ) is essential to occupants' health, comfort, and productivity [1–3]. IAQ is determined by various factors, among which the concentration of CO_2 is a critical one and is regarded as an indicator for IAQ [4]. To dilute indoor CO_2, ventilation, natural or mechanical, is the most common method [5]. However, ventilation, especially in the cooling and heating seasons, consumes a significant amount of energy. Currently, ventilation and related air treatment account for 40% to 60% of energy consumption in buildings [6].

The energy penalty of ventilation demands alternative solutions to IAQ. Removing CO_2 as a pollutant by using air cleaning technologies allows for acceptable indoor air quality while reducing the energy costs associated with ventilation. However, CO_2 has a relatively low boiling point of $-78.46\,^\circ\text{C}$, making it challenging to capture at room temperature. In recent years, the development of carbon capture technologies has been significantly boosted to combat climate change. CO_2 capture technologies include solid adsorption, liquid absorption, membrane purification, and cryogenic distillation [7,8], among which adsorption by porous solids has drawn enormous attention due to its lower energy consumption for regeneration [9–11]. Various forms of adsorption units, such as fixed bed and rotary adsorbents, have been developed to capture CO_2, and extensive research has been carried out on the optimization of adsorption materials and operation

processes [12–14]. Kim et al. [15,16] introduced a CO_2 adsorption capture device into a conventional ventilation system to mitigate the deterioration of air quality caused by residential breathing. With the advanced system, 30–60% of the ventilation energy consumption was saved. Thermodynamically, the possibility of carbon capture technology for achieving negative carbon was explored by Zhao et al. [17], and it was proposed that carbon capture technology can be a potential way to promote zero carbon building to negative carbon building. Shen et al. [18,19] combined the carbon capture system with low-grade energy and analyzed its performance in 20 global cities. Their results demonstrated the potential contribution of indoor carbon capture technology to carbon reduction and energy savings in building operations.

Due to the finite adsorption capacity of adsorbers, continuous adsorption is commonly implemented by cyclic processes such as temperature swing adsorption (TSA), pressure swing adsorption (PSA), or a combination of these two [20,21]. These processes involve altering the temperature or pressure conditions to control the adsorption and desorption of the target components on an adsorbent material. Different types of adsorber configurations were developed for the TSA and PSA processes, including fixed, rotating, and fluidized beds. The fixed and fluidized configurations require at least two beds to seamlessly alternate between adsorption and desorption, and they may be too cumbersome to be integrated in HVAC (heating, ventilation, and air conditioning) systems. In comparison, a rotating packed bed structure is more compact and has been widely used in HVAC systems for dehumidification [22,23] and heat recovery [24]. However, to our best knowledge, no studies have investigated the effect of a rotary adsorber on the continuous capture of indoor CO_2. In the present study, we aim to build up a coupled heat and mass transfer model to investigate how the rotating speed, velocity, and temperature of purging gas (desorption) and sectioning affect the outlet concentration and temperature.

2. Materials and Methods

2.1. Materials and Governing Equations

In order to complete the wheel adsorption simulation in ANSYS Fluent 2021R2 software, a user-defined function was written in the C language and linked to the program interface. UDF is mainly used to calculate the source terms of the mass and energy equations. The characteristics of Zeolite 13X are taken from the data reported in the literature, as shown in Table 1. The selected gas is a mixture of CO_2 and N_2, and the following reasonable assumptions are made [12,25]:

(1) The mixed gas follows the ideal gas law;
(2) Gas flow is unsteady laminar flow;
(3) The porosity of porous media has a uniform distribution;
(4) The physical properties of the adsorbent are constant;
(5) Linear driving force model for adsorption kinetics.

Table 1. The characteristics of Zeolite 13X.

Parameter	Description	Value	Unit	Source
D	Radius of rotor	1.0	m	
H	Height of rotor	0.2	m	
ε	Bed porosity	0.566		[26]
ε_p	Particle porosity	0.143		[27]
d_p	Particle diameter	0.0015	m	[26]
r_c	Crystal radius	5×10^{-10}	m	[27]
r_{pore}	Average pore radius	5.16×10^{-7}	m	[27]
ρ_s	Particle density	1230	kg/m^3	[26]
C_s	Adsorbent specific heat capacity	900	J/kg·K	[26]
λ_s	Adsorbent thermal conductivity	0.2	W/m·K	[26]

Table 1. *Cont.*

Parameter	Description	Value	Unit	Source
q_{m,CO_2}	CO_2 maximum adsorption capacity in adsorbent	9.842	mol/kg	[28]
K_{0,CO_2}	Adsorption constant at infinite dilution	6.89×10^{-9}	1/Pa	[28]
$\Delta H_{,CO_2}$	The heat of adsorption	30,371	J/mol	[28]
n	Toth model constant	$0.658 \times (0.0013 \times T)$		[28]
$x_{CO_2,ad,inlet}$	CO_2 adsorption inlet concentration	2000	ppm	
$x_{CO_2,de,inlet}$	CO_2 desorption inlet concentration	400	ppm	
$T_{ad,inlet}$	Adsorption inlet air temperature	293.15	K	
$T_{de,inlet}$	Desorption inlet air temperature	393.15	K	

2.1.1. Mass Conservation Equation

The mass conservation equation of each species in the fluid is expressed as:

$$\frac{\partial}{\partial t}\left(\varepsilon\rho_f y_i\right) + \nabla\cdot\left(\rho_f \vec{u} y_i\right) = \nabla\cdot\left(\varepsilon D_{ax,i}\nabla\rho_f y_i\right) - (1-\varepsilon)\rho_s M_i\frac{\partial q_i}{\partial t},$$

where y_i is the mass fraction of species i in fluid and $D_{ax,i}$ is the coefficient of the gas dispersion, m^2/s, and can be calculated by the following formula [29]:

$$\varepsilon\frac{D_{ax,i}}{D_{m,i}} = 20 + 0.5Sc_i Re_p,$$

where $D_{m,i}$ is the molecular diffusivity of species i, m^2/s; Sc_i is the Schmidt number; and Re_p is the Reynolds number.

The mass conservation equation of each species in the adsorbent can be expressed as:

$$\frac{\partial q_i}{\partial t} = k_{LDF,i}(q_i^* - q_i)$$

where $k_{LDF,i}$ is LDF mass transfer coefficient, s^{-1}; q_i^* is equilibrium adsorption capacity in adsorbent, mol/kg.

2.1.2. Energy Conservation Equation

The heat transfer models of porous media mainly include the local thermal equilibrium model and the local thermal non-equilibrium model. A non-dimensional number S_p, that is, the Sparrow number, was proposed by Minkowycz [30] for checking whether the local thermal equilibrium is applicable or not as follows:

$$S_p = \frac{2h_0 H^2}{\Gamma_{eff,s}\cdot D},$$

$$Pe = \frac{c_p u H}{\Gamma_{eff,s}}.$$

Only when S_p/Pe is large enough, such as $S_p/Pe > 100$, is local thermal equilibrium applicable. In this study, the value of S_p/Pe is much less than 100, so the local thermal non-equilibrium model is used.

The energy equation of a fluid can be expressed as:

$$\frac{\partial}{\partial t}\left(\varepsilon\rho_f C_p T_f\right) + \nabla\cdot\left(\rho_f C_p \vec{u} T_f\right) = \nabla\cdot\left(\Gamma_{eff,f}\nabla T_f\right) + h_{fs}A_{fs}\left(T_s - T_f\right),$$

where C_p is the specific heat of fluid, J/(kg·K); $\Gamma_{eff,f}$ is the effective thermal conductivity of fluid, W/(m·K); T_f is the temperature of fluid, K; T_s is the temperature of adsorbent, K; h_{fs} is the heat transfer coefficient for the fluid/solid interface, W/(m·K); and A_{fs} is interfacial area density, that is, the ratio of the area of the fluid/solid interface and the volume of the porous zone, m^{-1}.

The energy equation of an adsorbent can be expressed as:

$$\frac{\partial}{\partial t}\left[(1-\varepsilon)\rho_s C_s T_s\right] + \nabla\cdot\left[(1-\varepsilon)\rho_s C_s \overline{U} T_s\right] = \nabla\cdot\left[\Gamma_{eff,s}\nabla T_s\right] + h_{fs}A_{fs}\left(T_f - T_s\right) - (1-\varepsilon)\rho_s \sum_i \Delta H_i \frac{\partial q_i}{\partial t},$$

where C_s is the specific heat of the adsorbent, J/(kg·K); $\Gamma_{eff,s}$ is the effective thermal conductivity of adsorbent W/(m·K); and ΔH_i is the heat of the adsorption, J/mol.

The interstitial volumetric heat transfer coefficient, h_{fs}, between the fluid and matrix can be calculated by the following formula:

$$h_{fs} = \frac{6(1-\varepsilon)h_0}{d_p},$$

where h_0 is the overall heat transfer coefficient of the porous matrix:

$$Nu = \frac{h_0 d_p}{\lambda_f} = 2.0 + 1.1Re_p^{0.6}Pr^{1/3}.$$

The effective thermal conductivity of fluids and solids can be calculated using the following formula:

$$\Gamma_{eff,f} = \varepsilon\lambda_f,$$

$$\Gamma_{eff,s} = (1-\varepsilon)\lambda_s,$$

where λ_f is the thermal conductivity of fluids, W/(m·K), and λ_s is the thermal conductivity of solids, W/(m·K).

2.2. Adsorption Isotherms and Kinetics

The adsorption isotherms of Zeolite 13X were estimated by the Toth model [28]:

$$q_i^* = \frac{q_{m,i}K_{eq,i}p_i}{\left(1 + \left(K_{eq,i}p_i\right)^n\right)^{\frac{1}{n}}},$$

where q_i^* is the equilibrium adsorption capacity in the adsorbent, mol/kg; $q_{m,i}$ is the maximum adsorption capacity in the adsorbent, mol/kg; n is the model constant; and $K_{eq,i}$ is the equilibrium adsorption constant, Pa^{-1}, which can be calculated by the following formula:

$$K_{eq,i} = K_{0,i}e^{\left(-\frac{\Delta H_i}{RT_f}\right)},$$

where $K_{0,i}$ is the adsorption constant at infinite dilution, Pa^{-1}; ΔH_i is the heat of adsorption, J/mol; R is the gas constant, J/(mol·K); T_f is the temperature of the fluid, K; and p_i is the partial pressure of species i in the fluid, Pa, which can be calculated by the following formula:

$$\rho_f y_i = \frac{p_i}{R_{g,i}T_f},$$

where ρ_f is the density of the fluid, kg/m^3; y_i is the mass fraction of species i in the fluid; $R_{g,i}$ is the gas constant for the species i, J/(kg·K); and T_f is the temperature of the fluid, K.

The LDF mass transfer coefficient $k_{LDF,i}$ consists of three parts: the film resistance, the macropore diffusion, and the micropore diffusion.

$$\frac{1}{k_{LDF,i}} = \frac{r_p}{3k_{f,i}}\frac{q_0}{c_0} + \frac{r_p^2}{15\varepsilon D_{eff,i}}\frac{q_0}{c_0} + \frac{r_c^2}{15D_c},$$

where $k_{LDF,i}$ is the LDF mass transfer coefficient, s^{-1}; r_p is the radius of the adsorbent particles, m; r_c is the average radius of the adsorbent crystals, m; ε is the porosity of the adsorbent particle; k_f is the film resistance coefficient for species i, s^{-1}; $D_{eff,i}$ is the effective diffusion coefficient, including molecular diffusion and Knudsen diffusion, m^2/s; D_c is the microporous diffusion coefficient, m^2/s; and q_0 is the CO_2 concentration in the solid phase at adsorption equilibrium, mol/m^3, which can be obtained by the adsorption isotherm equation; c_0 is the CO_2 concentration in the gas phase at adsorption equilibrium, mol/m^3, and converting the gas phase concentration units.

The effective diffusion coefficient $D_{eff,i}$ in the adsorbent particles can be calculated by the following equation:

$$\frac{1}{D_{eff,i}} = \tau\left(\frac{1}{D_{K,i}} + \frac{1}{D_{m,i}}\right),$$

where τ is the tortuosity factor and $D_{K,i}$ is the Knudsen diffusion coefficient of species i, m^2/s, which is obtained by the following formula:

$$D_{K,i} = \frac{2r_{pore}}{3}\left(\frac{8RT}{\pi M_i}\right)^{0.5},$$

where r_{pore} is the average radius of the adsorbent crystals, m; $D_{m,i}$ is the molecular diffusion coefficient of species i, m^2/s; and M_i is the molecular weight of species i, kg/mol.

The film resistance coefficient $k_{f,i}$ can be obtained using the following formula:

$$k_{f,i} = \frac{Sh_i D_{m,i}}{d_p}.$$

The Sherwood number can be calculated using the following formula:

$$Sh_i = 2.0 + 1.1Re_p^{0.6}Sc_i^{1/3}.$$

The Reynolds number Re_p, the Schmidt number Sc_i, and the Prandtl number Pr can be obtained using the following formulas:

$$Re_p = \frac{\rho_f d_p |u|}{\mu},$$

$$Sc_i = \frac{\mu}{\rho_f D_{m,i}},$$

$$Pr = \frac{c_p \mu}{\lambda_f}.$$

2.3. Boundary and Initial Conditions

2.3.1. Boundary Conditions

Only the heat and mass transfer process of the rotor is considered, and the heat and mass exchange with the outside world is not considered. Therefore, the temperature gradient and concentration gradient on the inlet and outlet boundaries and the inner and outer walls of the rotor are both zero. The temperature, velocity, and CO_2 concentration of the adsorption inlet are the values of typical indoor scenes (such as classrooms), while the

desorption inlet concentration selects the most common atmospheric CO_2 concentration value. The expression of boundary conditions is shown in Table 2.

Table 2. Boundary conditions.

At the Inlet	At the Outlet	On the Inner and Outer Walls
$T_f = T_{f,in}$	$\dfrac{dT_f}{dz} = 0$	$\dfrac{dT_f}{dr} = 0$
$\dfrac{dT_s}{dz} = 0$	$\dfrac{dT_s}{dz} = 0$	$\dfrac{dT_s}{dr} = 0$
$u = u_{f,in}$	$\dfrac{du_f}{dz} = 0$	$u_r = 0$
$y_i = y_{i,in}$	$\dfrac{dy_i}{dz} = 0$	$\dfrac{dy_i}{dz} = 0$
$\dfrac{dq_i}{dz} = 0$	$\dfrac{dq_i}{dz} = 0$	$\dfrac{dq_i}{dz} = 0$

2.3.2. Initial Conditions

Assuming that the rotor has reached a balanced and stable state with the ambient air before operation, the initial gas phase and solid phase temperatures in the rotor are both ambient temperatures, the initial gas phase concentration is the ambient CO_2 concentration, and the initial adsorption amount is the equilibrium adsorption amount corresponding to the ambient CO_2 concentration. Therefore, the initial conditions are determined as shown in Table 3.

Table 3. Initial conditions.

Temperature	Species Mass Fraction	Adsorbed Amount
$T_{s,0} = T_{env}$ $T_{f,0} = T_{env}$	$y_{i,0} = y_{i,env}$	$q_{i,0} = q_{i,0}^* = \dfrac{q_{m,i} K_{eq,i,0} p_{i,0}}{\left(1 + \left(K_{eq,i,0} p_{i,0}\right)^n\right)^{\frac{1}{n}}}$ $K_{eq,i,0} = K_{0,i} e^{\left(-\frac{\Delta H_i}{R T_{f,0}}\right)}$ $\rho_f y_{i,0} = \dfrac{p_{i,0}}{R_{g,i} T_{f,0}}$

2.4. Solve the Settings and Grid Independence Test

The ideal gas law was used to calculate the density of the mixed gas. To calculate the thermal conductivity and dynamic viscosity of the mixed gas, the mass-weighted mixing law was applied. The ANSYS Fluent solver incorporated the mass conservation equation of the adsorbent through User-Defined Scalars. The pressure-velocity coupling field was solved using the SIMPLE algorithm. The gradient term and convection term were discretized using the least squares cell-based scheme and the second-order upwind scheme, respectively. A grid independence test was conducted, and based on accuracy and computational cost considerations, a grid size of 262,000 was chosen for the calculations. Figure 1a illustrates the variations in average CO_2 concentration and temperature at the adsorption outlet. Figure 1b displays the mesh used in the computational analysis conducted in this study.
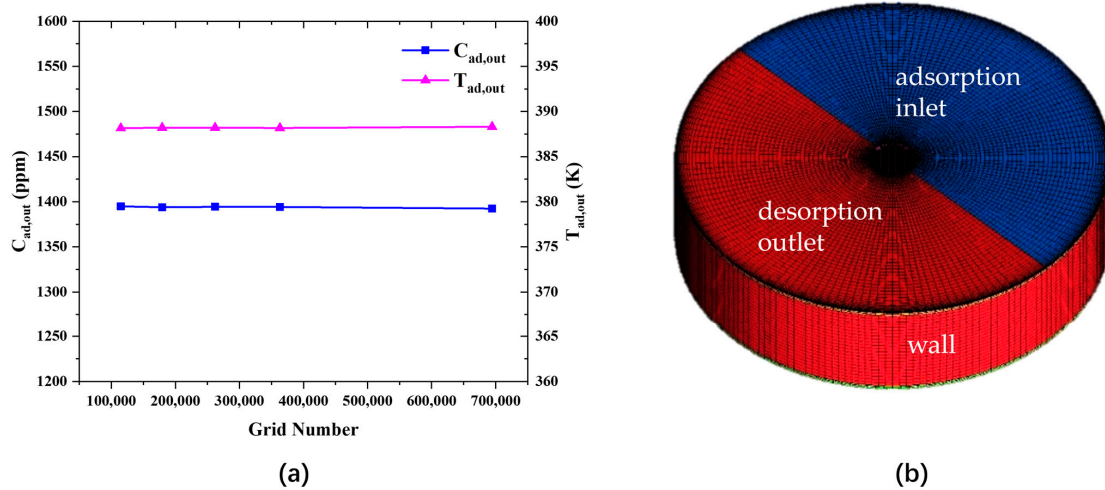
(a)

(b)

Figure 1. (**a**) Grid independence test; (**b**) mesh for the computation.

3. Results and Discussion

3.1. Temperature and Concentration Distribution in the Wheel

In the adsorption wheel device, the adsorbent wheel is subjected to cooling and heating through the airflow passing through the adsorption and desorption zones, respectively. Concurrently, the adsorbent material undergoes successive adsorption and desorption processes as the wheel rotates in a clockwise manner, opposite to the Y-axis direction, thereby completing the cycle for CO_2 capture. As depicted in Figure 2, the fluid concentration distribution (Figure 2a), fluid temperature distribution (Figure 2b), adsorbed CO_2 distribution within the adsorbent (Figure 2c), and solid-phase temperature distribution within the adsorbent (Figure 2d) are illustrated. The findings reveal that the fluid concentration distribution displays stratification into distinct zones, exhibiting a gradient in the rotational direction. Notably, the energy content of the fluid and solid phases differs solely in terms of adsorption heat, with the gas-solid heat transfer coefficient being relatively high and the adsorption heat being minimal. Consequently, the gas-phase and solid-phase temperatures exhibit a comparable distribution pattern. Furthermore, the distribution of solid-phase concentration is influenced by both the temperature and partial pressures of the components.
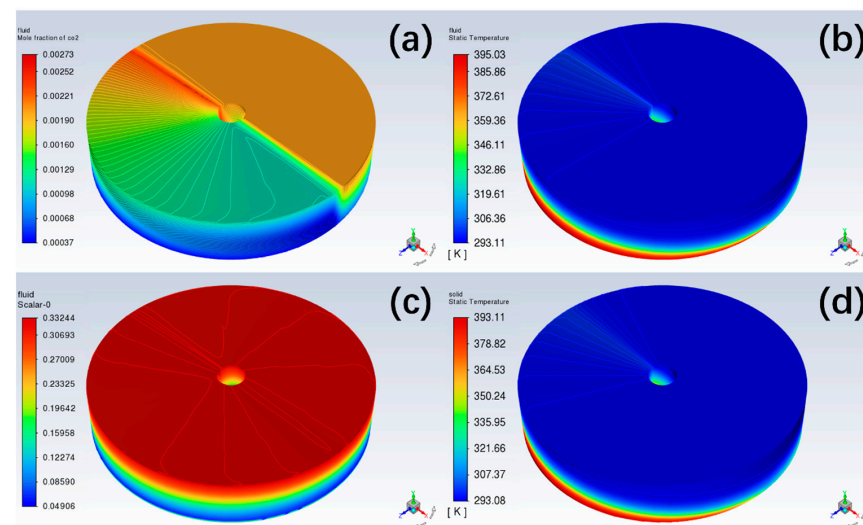

Figure 2. Distributions of molar concentration of CO_2 (**a**); fluid temperature (**b**); adsorption amount of CO_2 (**c**); and adsorbent temperature (**d**). (13X ω = 0.5 r/min, $T_{ad,in}$ = 293.15 K, $T_{de,in}$ = 393.15 K, $V_{ad,in}$ = 1 m/s, $V_{de,in}$ = 1 m/s).

3.2. Effect of Rotating Speed

Figure 3 shows the results of gas-phase CO_2 concentration and temperature distribution under different rotational speeds. It is evident that the average concentration and temperature at the adsorption outlet exhibit a gradient change along the rotational direction. As the rotational speed increases from 0.5 r/min to 2 r/min, the concentration gradient at the adsorption outlet in the rotational direction gradually decreases, and the maximum concentration value decreases as well. The temperature follows a similar pattern, gradually decreasing along the rotational direction. This is because as the rotation speed increases, the gas-solid contact time in the adsorption sector decreases, resulting in a smaller concentration difference at the outlet gas flow. The temperature change is similar. At higher rotation speeds, the outlet temperature distribution in the adsorption sector is more uniform with a lower extreme difference. Similar phenomena were observed in Tang et al.'s study [12].
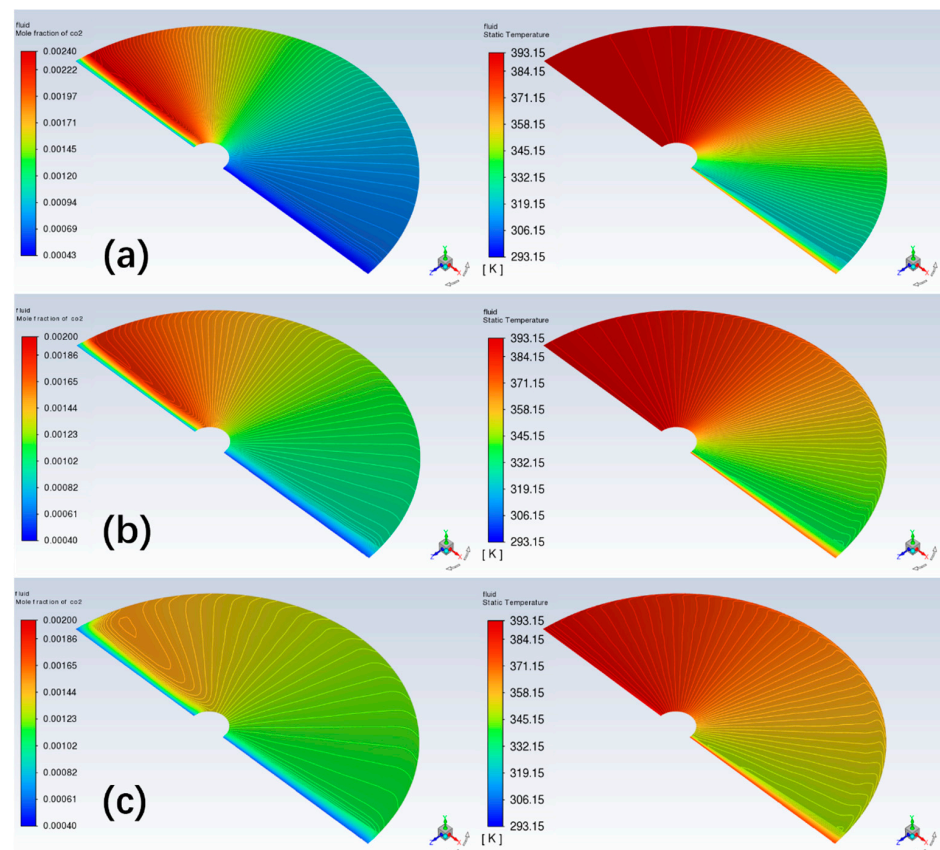

Figure 3. Contour of the mole fraction of CO_2 (**left**) and temperature (**right**) on the adsorption outlet at different rotating speeds: (**a**) 0.5 r/min; (**b**) 1 r/min; and (**c**) 2 r/min. (13X $T_{ad,in}$ = 293.15 K, $T_{de,in}$ = 393.15 K, $V_{ad,in}$ = 1 m/s, $V_{de,in}$ = 1 m/s).

Figure 4 shows the variation in outlet concentration and temperature at different rotational speeds. For the concentration distribution, although Figure 3 shows that increasing rotation speed made the outlet concentration distribution more uniform, Figure 4 shows that the average outlet concentrations for the rotating speed ranging from 0.5 to 3 r/min eventually converged to the same level. This may be because the axial flow velocity of the process air entering the wheel is the same for all conditions. Therefore, the contact time with the adsorbent in the axial direction during passage through the wheel device is the same, resulting in consistent average outlet concentrations, while the rotation speed only affects the circumferential concentration distribution and does not impact the average concentration value. However, the different circumferential concentration distributions can also be utilized by properly arranging the gas flow channels at the outlet to obtain air

streams with desired CO_2 concentrations [12]. For temperature distribution, the average adsorption and desorption outlet temperatures are almost the same for different rotation speeds, with very small temperature fluctuations caused by different speeds. This is because when the rotation speed is high enough, the adsorption outlet surface is dominated by the rotation effect. The inlet air flow of the desorption sector on the same side is affected by the rotation, causing changes in the adsorption outlet temperature and making it closer to the desorption inlet temperature. Similarly, the desorption outlet temperature will also be very close to the adsorption inlet temperature.
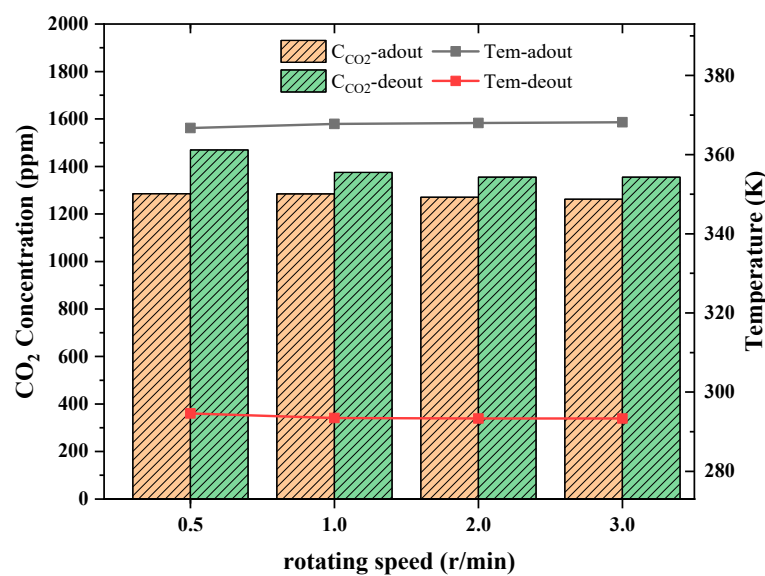
Figure 4. Effect of the rotating speed on the concentration of CO_2 and temperature at the outlet (13X $T_{ad,in}$ = 293.15 K, $T_{de,in}$ = 393.15 K, $V_{ad,in}$ = 1 m/s, $V_{de,in}$ = 1 m/s).

3.3. Effect of Desorption Inlet Velocity

Figures 5 and 6 depict the average concentration and temperature at the outlets under different desorption inlet flow rates. As the desorption inlet velocity increased, the average temperature at the desorption outlet also increased. This is because as the flow rate increases, the heat transfer area per unit mass flow rate decreases, resulting in reduced heat transfer performance of the rotary wheel and the desorption outlet temperature getting closer to the desorption inlet temperature. As to the adsorption outlet temperatures, except for the case of 1 m/s, they were around 391 K (close to the desorption inlet gas temperature) regardless of the desorption inlet velocity. Since the adsorption inlet velocity is 1 m/s, with a desorption inlet velocity higher than 1 m/s, the overall heat accumulating in the rotary wheel would increase. Therefore, the high temperature region below in Figure 7 will be much larger than the low temperature region above. Additionally, due to the rotation, the temperature distribution on the same side will be more uniform, i.e., the temperature distribution shows axial layering. The adsorption outlet sector will also be affected by the desorption inlet sector on the same plane, making the adsorption outlet temperature close to the desorption inlet temperature.

The desorption outlet concentration decreased significantly as the desorption inlet velocity increased. This is because the increase in desorption inlet velocity reduced the gas-solid contact time in the desorption sector and also elevated the temperature in the desorption sector. It is known from the characteristics of adsorption isotherms that the higher the temperature, the lower the adsorption capacity. As the desorption outlet temperature increases with the desorption flow rate, the temperature difference between the desorption inlet and outlet diminishes, resulting in a smaller working capacity of the adsorbent released and thus a lower average concentration at the desorption outlet.
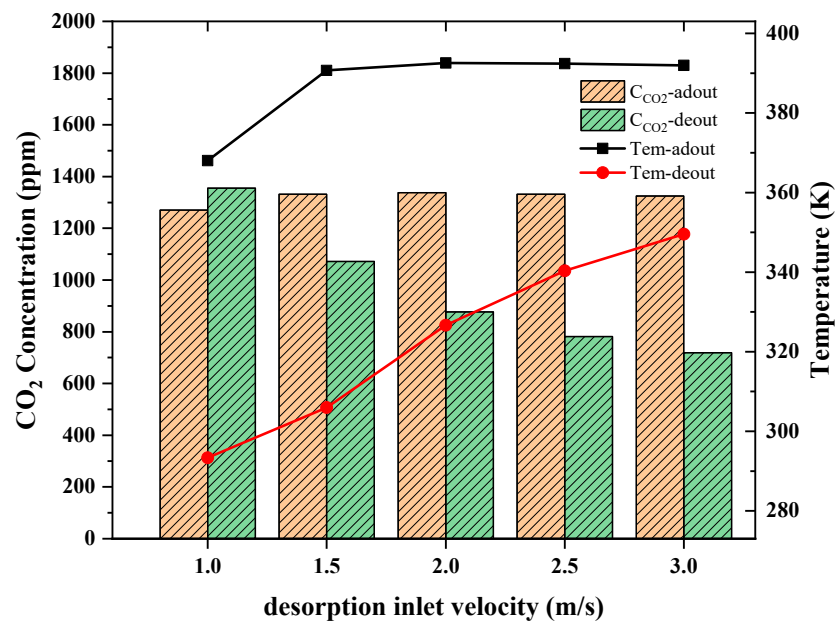
Figure 5. Variation of the outlet averaged concentration of CO_2 and temperature at the outlet with different desorption inlet velocities. (13X ω = 2 r/min, $T_{ad,in}$ = 293.15 K, $T_{de,in}$ = 393.15 K, $V_{ad,in}$ = 1 m/s).
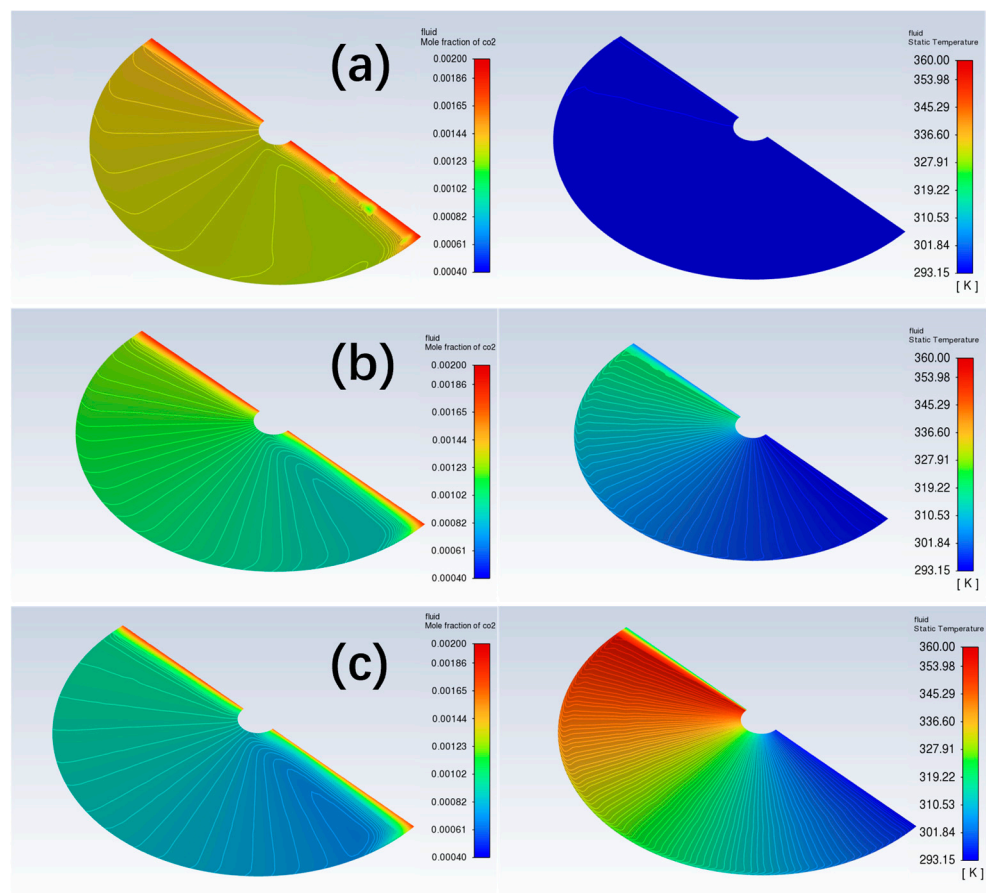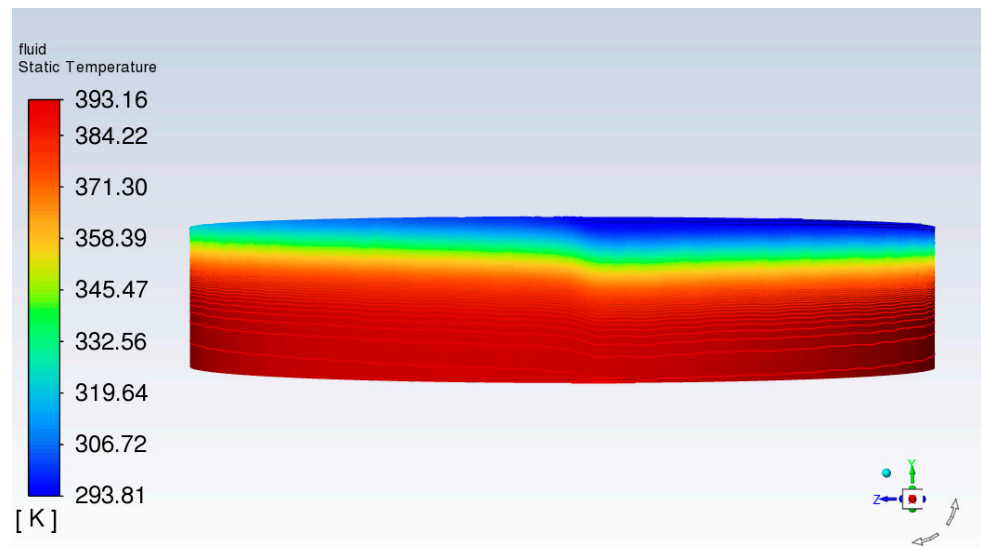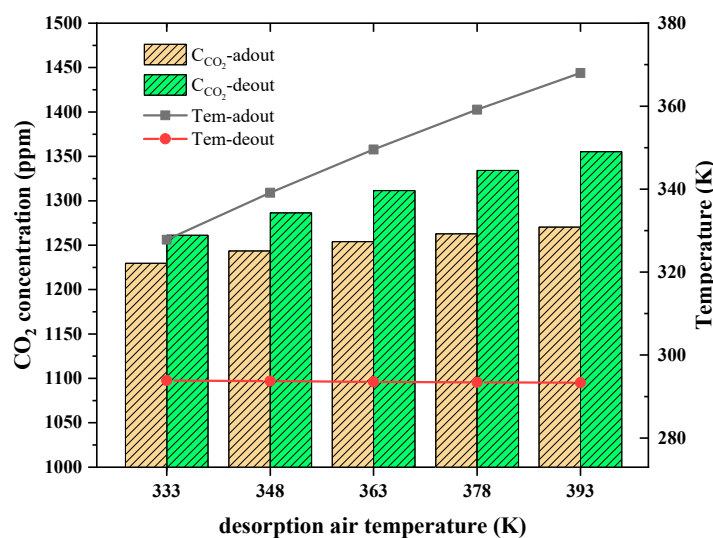

Figure 6. Contour of the mole fraction of CO_2 (**left**) and temperature (**right**) on the desorption outlet at different desorption inlet velocities: (**a**) 1 m/s; (**b**) 1.5 m/s; (**c**) 2 m/s. (13X ω = 2 r/min, $T_{ad,in}$ = 293.15 K, $T_{de,in}$ = 393.15 K, $V_{ad,in}$ = 1 m/s).

Figure 7. Axial distribution of temperature. (13X ω = 2 r/min, $T_{ad,in}$ = 293.15 K, $T_{de,in}$ = 393.15 K, $V_{ad,in}$ = 1 m/s, $V_{de,in}$ = 2 m/s).

3.4. Effect of Desorption Air Temperature

Figures 8 and 9 depict the variations in average temperature and concentration at the adsorption outlet in response to different temperatures of desorption airflow. Notably, an increase in the desorption inlet temperature yields a significant rise in the average temperature observed at the adsorption outlet. As mentioned before, this is mainly due to the rotation of the wheel, given that the adsorption outlet and desorption inlet are on the same plane. Consequently, the real-time temperature at the adsorption outlet closely approximates the temperature of the desorption inlet airflow. Similarly, the temperature at the desorption outlet exhibits a similar proximity to the temperature observed at the adsorption inlet. In addition, the increase in the desorption temperature also led to more heat entering the rotary wheel device, raising the overall temperature of the wheel. The temperature increase reduces the CO_2 adsorption capacity of the adsorbent, resulting in a higher outlet concentration for the adsorption sector and more desorbed CO_2, giving a higher desorption outlet concentration. Similar phenomena were also observed in a previous study [31].

**Figure 8.** Effect of the desorption inlet air temperature on the adsorption amount and temperature at the adsorption outlet (13X ω = 2 r/min, $T_{ad,in}$ = 293.15 K, $V_{ad,in}$ = 1 m/s, $V_{de,in}$ = 1 m/s).
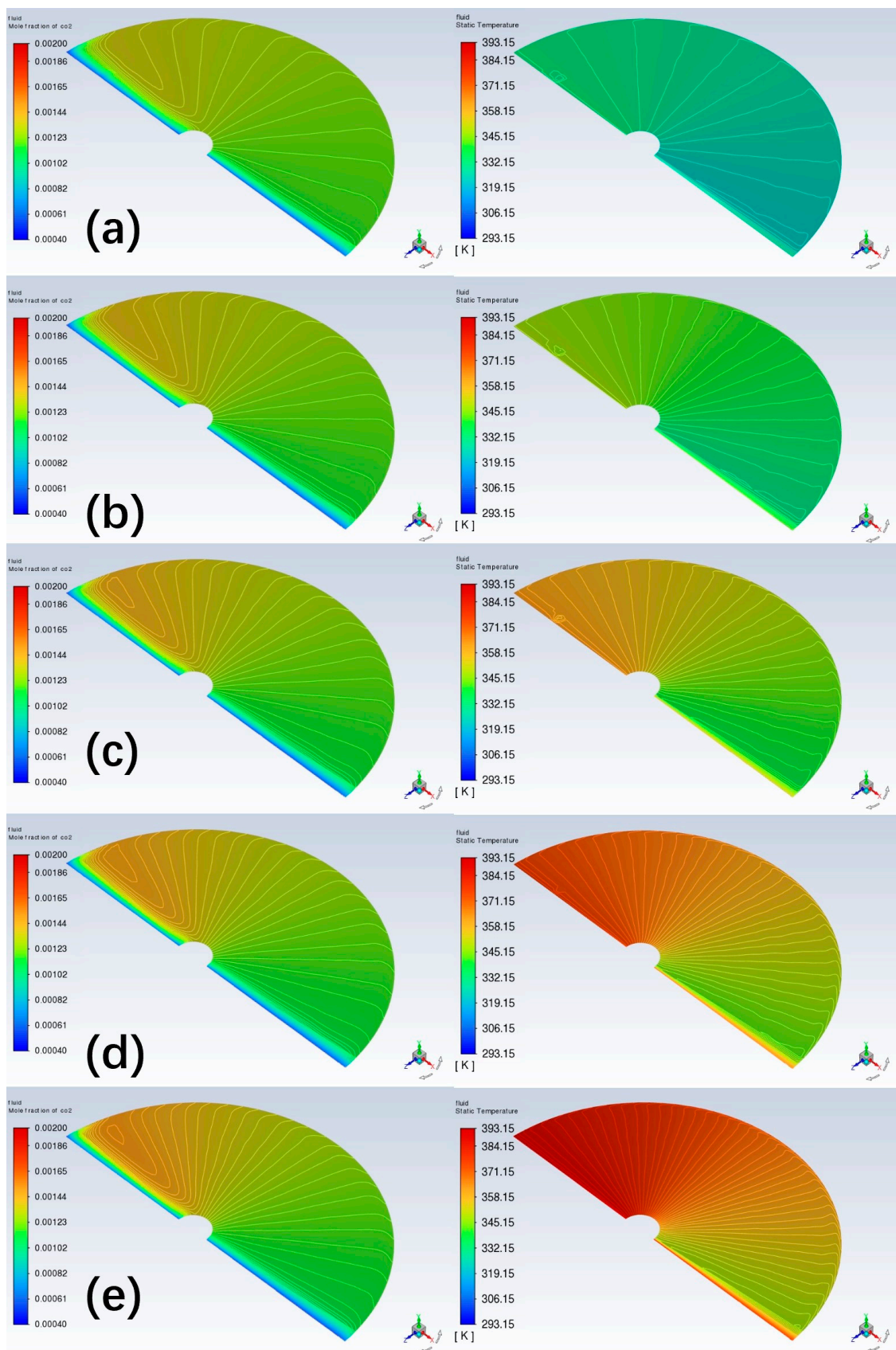
Figure 9. Contour of the mole fraction of CO_2 (left) and temperature (right) on the adsorption outlet at different desorption air temperatures: (**a**) 333 K; (**b**) 348 K; (**c**) 363 K; (**d**) 378 K; and (**e**) 393 K. (13X ω = 2 r/min, $T_{ad,in}$ = 293.15 K, $V_{ad,in}$ = 1 m/s, $V_{de,in}$ = 1 m/s).
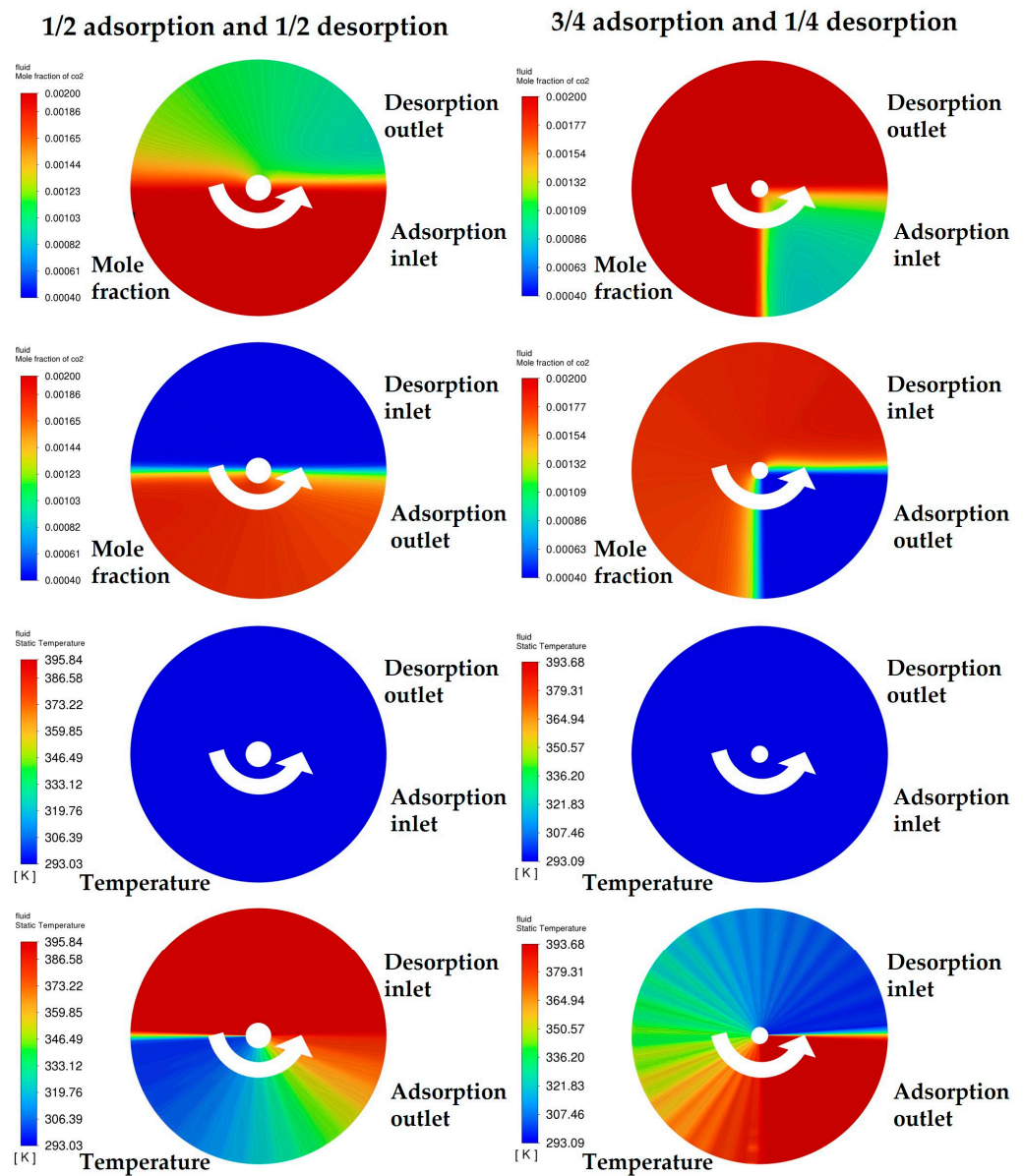
3.5. Different Proportion of Desorption Zone

Figures 10 and 11 provide a visual representation of the average concentration and temperature at the outlets, considering two distinct desorption zone ratios. It should be noted that the adsorbents in Figures 10 and 11 have an average particle diameter of 0.002 m compared to 0.0015 m in previous figures, and different mass transfer coefficient values are given. The findings reveal that, while maintaining identical adsorption and desorption airflow rates, a slight increase in the average concentration at the adsorption outlet and a marginal decrease in the average concentration at the desorption outlet are observed when the desorption zone ratio shifts from 1/2 to 1/4. Conversely, the average temperature at the outlets remains nearly constant for both zone configurations. The primary consequence of altering the desorption zone ratio from 1/2 to 1/4 is an augmented desorption inlet airflow rate combined with a diminished adsorption inlet airflow rate. As discussed earlier, the desorption inlet airflow rate significantly influences the concentration at the desorption outlet, resulting in a lower average concentration relative to the 1/2 zone configuration. A similar principle can account for the slight increase in average concentration at the adsorption outlet, which is attributed to the reduction in the adsorption inlet airflow rate. Consequently, the disparate rates of change in outlet velocities engender different rates of change in outlet concentrations.
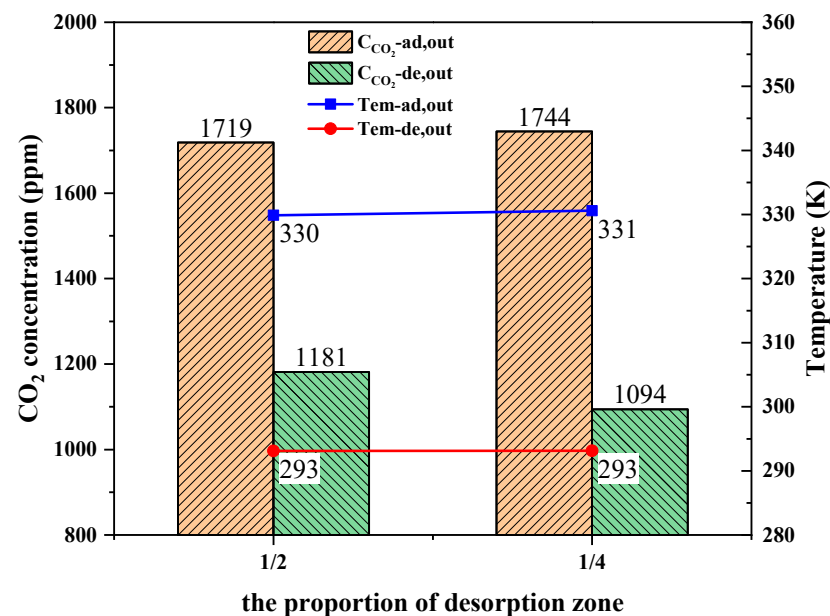
Figure 10. Variation of the outlet average concentration of CO_2 and temperature at the outlet with different proportions of the desorption zone. (13X ω = 2 r/min, $T_{ad,in}$ = 293.15 K, $T_{de,in}$ = 393.15 K; $V_{ad,in}$ = 3 m/s; and $V_{de,in}$ = 1.5 m/s when the proportion of desorption zone is 1/2, or $V_{ad,in}$ = 2 m/s and $V_{de,in}$ = 3 m/s when the proportion of desorption zone is 1/4).

Similarly, in line with the impact of rotational speed, when the wheel's rotational speed reaches 2 r/min, the average temperature at the desorption outlet closely approximates the temperature at the adsorption inlet. Given the same inlet airflow rate, the heat flow into and out of the fluid should remain equal. When the desorption outlet temperature aligns with the adsorption inlet temperature, it becomes evident that the average temperature at the adsorption outlet should also be comparable. Since the desorption inlet average temperatures are equivalent for both zone configurations, it follows that the average temperature at the adsorption outlet should likewise exhibit similarity.

Figure 11. Contour of the mole fraction of CO_2 and temperature on the adsorption outlet at different proportions of the desorption zone. (13X ω = 2 r/min, $T_{ad,in}$ = 293.15 K, $T_{de,in}$ = 393.15 K).

4. Conclusions

The present study investigated a regenerative rotary adsorber for indoor CO_2 capture by modeling the coupled heat and mass transfer processes within the adsorber. The key findings are:

(1) In the rotation speed range of 0.5–3 rpm, adjusting the speed mainly affects circumferential concentration and temperature distribution but has little impact on axial concentration and temperature;

(2) Increasing desorption inlet flow rate has little impact on adsorption outlet concentration but significantly decreases desorption outlet concentration. Increasing the desorption inlet flow rate also significantly raises the desorption outlet temperature but has little impact on the adsorption outlet temperature when the desorption inlet flow rate is 1.5 m/s or higher;

(3) Raising the desorption inlet temperature increases both adsorption and desorption outlet average concentrations. Increasing desorption inlet temperature also significantly increases adsorption outlet temperature but has little impact on desorption outlet temperature;

(4) Reducing the volume proportion of the desorption sector slightly increases adsorption outlet concentration, slightly decreases desorption outlet concentration, but barely affects average adsorption and desorption outlet temperatures.

Institutional Review Board Statement: The study was approved by the Institutional Review Board of Chongqing University.

Informed Consent Statement: Not applicable.

Data Availability Statement: Not applicable.

Conflicts of Interest: The authors declare no conflict of interest.

References

1. Hahn Menacho, Á.J.; Marvuglia, A.; Benetto, E. Occupant's health and energy use in an office building: A sensor-enabled life cycle assessment. *Build. Environ.* **2023**, *236*, 110274. [CrossRef]
2. Park, J.; Loftness, V.; Aziz, A.; Wang, T.-H. Critical factors and thresholds for user satisfaction on air quality in office environments. *Build. Environ.* **2019**, *164*, 106310. [CrossRef]
3. Yin, H.; Zhai, X.; Ning, Y.; Li, Z.; Ma, Z.; Wang, X.; Li, A. Online monitoring of PM2.5 and CO_2 in residential buildings under different ventilation modes in Xi'an city. *Build. Environ.* **2021**, *207*, 108453. [CrossRef]
4. Persily, A. Development and application of an indoor carbon dioxide metric. *Indoor Air* **2022**, *32*, e13059. [CrossRef]
5. Li, B.; Cai, W. A novel CO_2-based demand-controlled ventilation strategy to limit the spread of COVID-19 in the indoor environment. *Build. Environ.* **2022**, *219*, 109232. [CrossRef] [PubMed]
6. Rajan, P.E.; Krishnamurthy, A.; Morrison, G.; Rezaei, F. Advanced buffer materials for indoor air CO_2 control in commercial buildings. *Indoor Air* **2017**, *27*, 1213–1223. [CrossRef] [PubMed]
7. Choi, S.; Gray, M.L.; Jones, C.W. Amine-Tethered Solid Adsorbents Coupling High Adsorption Capacity and Regenerability for CO_2 Capture from Ambient Air. *Chemsuschem* **2011**, *4*, 628–635. [CrossRef]
8. Lee, S.-Y.; Park, S.-J. A review on solid adsorbents for carbon dioxide capture. *J. Ind. Eng. Chem.* **2015**, *23*, 1–11. [CrossRef]
9. An, X.; Li, T.; Chen, J.; Fu, D. 3D-hierarchical porous functionalized carbon aerogel from renewable cellulose: An innovative solid-amine adsorbent with high CO_2 adsorption performance. *Energy* **2023**, *274*, 127392. [CrossRef]
10. Mazaj, M.; Bjelica, M.; Žagar, E.; Logar, N.Z.; Kovacic, S. Zeolite Nanocrystals Embedded in Microcellular Carbon Foam as a High-Performance CO_2 Capture Adsorbent with Energy-Saving Regeneration Properties. *Chemsuschem* **2020**, *13*, 2089–2097. [CrossRef]
11. Wang, X.; Zeng, W.; Song, M.; Wang, F.; Hu, X.; Guo, Q.; Liu, Y. Polyetheramine improves the CO_2 adsorption behavior of tetraethylenepentamine-functionalized sorbents. *Chem. Eng. J.* **2019**, *364*, 475–484. [CrossRef]
12. Tang, C.; Gao, X.; Shao, Y.; Wang, L.; Liu, K.; Gao, R.; Che, D. Investigation on the rotary regenerative adsorption wheel in a new strategy for CO_2 enrichment in greenhouse. *Appl. Therm. Eng.* **2022**, *205*, 118043. [CrossRef]
13. Chaffee, A.L.; Knowles, G.P.; Liang, Z.; Zhang, J.; Xiao, P.; Webley, P.A. CO_2 capture by adsorption: Materials and process development. *Int. J. Greenh. Gas Control.* **2007**, *1*, 11–18. [CrossRef]
14. Bui, M.; Adjiman, C.S.; Bardow, A.; Anthony, E.J.; Boston, A.; Brown, S.; Fennell, P.S.; Fuss, S.; Galindo, A.; Hackett, L.A.; et al. Carbon capture and storage (CCS): The way forward. *Energy Environ. Sci.* **2018**, *11*, 1062–1176. [CrossRef]
15. Kim, M.K.; Baldini, L.; Leibundgut, H.; Wurzbacher, J.A.; Piatkowski, N. A novel ventilation strategy with CO_2 capture device and energy saving in buildings. *Energy Build.* **2015**, *87*, 134–141. [CrossRef]
16. Kim, M.K.; Baldini, L.; Leibundgut, H.; Wurzbacher, J.A. Wurzbacher, Evaluation of the humidity performance of a carbon dioxide (CO_2) capture device as a novel ventilation strategy in buildings. *Appl. Energy* **2020**, *259*, 112869. [CrossRef]
17. Zhao, R.; Liu, L.; Zhao, L.; Deng, S.; Li, S.; Zhang, Y.; Li, H. Thermodynamic exploration of temperature vacuum swing adsorption for direct air capture of carbon dioxide in buildings. *Energy Convers. Manag.* **2019**, *183*, 418–426. [CrossRef]
18. Shen, Y.; Yang, H. Global performance analysis of a solar-driven indoor CO_2/H_2O capture system for air quality enhancement and cooling energy saving. *Energy Convers. Manag.* **2023**, *280*, 116831. [CrossRef]
19. Shen, Y.; Yang, H. Multi-Objective Optimization of Integrated Solar-Driven CO_2 Capture System for an Industrial Building. *Sustainability* **2023**, *15*, 526.

20.   Dhoke, C.; Cloete, S.; Krishnamurthy, S.; Seo, H.; Luz, I.; Soukri, M.; Park, Y.-K.; Blom, R.; Amini, S.; Zaabout, A. Sorbents screening for post-combustion CO_2 capture via combined temperature and pressure swing adsorption. *Chem. Eng. J.* **2020**, *380*, 122201. [CrossRef]

21.   Mason, J.A.; Sumida, K.; Herm, Z.R.; Krishna, R.; Long, J.R. Evaluating metal-organic frameworks for post-combustion carbon dioxide capture via temperature swing adsorption. *Energy Environ. Sci.* **2011**, *4*, 3030–3040. [CrossRef]

22.   Ge, T.; Ziegler, F.; Wang, R. A mathematical model for predicting the performance of a compound desiccant wheel (A model of compound desiccant wheel). *Appl. Therm. Eng.* **2010**, *30*, 1005–1015. [CrossRef]

23.   Alabi, W.O.; Karoyo, A.H.; Krishnan, E.N.; Dehabadi, L.; Wilson, L.D.; Simonson, C.J. Comparison of the Moisture Adsorption Properties of Starch Particles and Flax Fiber Coatings for Energy Wheel Applications. *ACS Omega* **2020**, *5*, 9529–9539. [CrossRef] [PubMed]

24.   Wang, L.; Wang, C.; Guo, Y.; Wu, Y.; Bai, W.; Che, D. Novel rotary regenerative heat exchanger using cascaded phase change material capsules. *Appl. Therm. Eng.* **2021**, *188*, 116619. [CrossRef]

25.   Wang, L.; He, Y.; Tang, C.; Wang, Y.; Che, D. A novel design of rotary regenerative condensing heat exchanger for the dehydration from high humidity flue gas. *Int. J. Heat Mass Transf.* **2019**, *131*, 517–526. [CrossRef]

26.   Qasem, N.A.A.; Ben-Mansour, R. Adsorption breakthrough and cycling stability of carbon dioxide separation from $CO_2/N_2/H_2O$ mixture under ambient conditions using 13X and Mg-MOF-74. *Appl. Energy* **2018**, *230*, 1093–1107. [CrossRef]

27.   Hu, X.; Mangano, E.; Friedrich, D.; Ahn, H.; Brandani, S. Diffusion mechanism of CO_2 in 13X zeolite beads. *Adsorption* **2014**, *20*, 121–135. [CrossRef]

28.   Cavenati, S.; Grande, C.A.; Rodrigues, A.E. Rodrigues, Adsorption Equilibrium of Methane, Carbon Dioxide, and Nitrogen on Zeolite 13X at High Pressures. *J. Chem. Eng. Data* **2004**, *49*, 1095–1101. [CrossRef]

29.   Qazvini, O.T.; Fatemi, S. Modeling and simulation pressure-temperature swing adsorption process to remove mercaptan from humid natural gas; a commercial case study. *Sep. Purif. Technol.* **2015**, *139*, 88–103. [CrossRef]

30.   Minkowycz, W.; Haji-Sheikh, A.; Vafai, K. On departure from local thermal equilibrium in porous media due to a rapidly changing heat source: The Sparrow number. *Int. J. Heat Mass Transf.* **1999**, *42*, 3373–3385. [CrossRef]

31.   Herraiz, L.; Palfi, E.; Fernández, E.S.; Lucquiaud, M. Lucquiaud, Rotary Adsorption: Selective Recycling of CO_2 in Combined Cycle Gas Turbine Power Plants. *Front. Energy Res.* **2020**, *8*, 482708. [CrossRef]